

Structural basis of complex formation between mitochondrial anion channel VDAC1 and Hexokinase-II

Nandan Haloi^{1,2,3}, Po-Chao Wen^{1,2,3}, Qunli Cheng⁴, Meiying Yang⁴, Gayathri Natarajan⁴, Amadou K. S. Camara^{4,5,6}, Wai-Meng Kwok^{4,6,7}✉ & Emad Tajkhorshid^{1,2,3}✉

Complex formation between hexokinase-II (HKII) and the mitochondrial VDAC1 is crucial to cell growth and survival. We hypothesize that HKII first inserts into the outer membrane of mitochondria (OMM) and then interacts with VDAC1 on the cytosolic leaflet of OMM to form a binary complex. To systematically investigate this process, we devised a hybrid approach. First, we describe membrane binding of HKII with molecular dynamics (MD) simulations employing a membrane mimetic model with enhanced lipid diffusion capturing membrane insertion of its H-anchor. The insertion depth of the H-anchor was then used to derive positional restraints in subsequent millisecond-scale Brownian dynamics (BD) simulations to preserve the membrane-bound pose of HKII during the formation of the HKII/VDAC1 binary complex. Multiple BD-derived structural models for the complex were further refined and their structural stability probed with additional MD simulations, resulting in one stable complex. A major feature in the complex is the partial (not complete) blockade of VDAC1's permeation pathway, a result supported by our comparative electrophysiological measurements of the channel in the presence and absence of HKII. We also show how VDAC1 phosphorylation disrupts HKII binding, a feature that is verified by our electrophysiology recordings and has implications in mitochondria-mediated cell death.

¹Theoretical and Computational Biophysics Group, NIH Center for Macromolecular Modeling and Bioinformatics, Beckman Institute for Advanced Science and Technology, University of Illinois at Urbana-Champaign, Urbana, IL, USA. ²Department of Biochemistry, University of Illinois at Urbana-Champaign, Urbana, IL, USA. ³Center for Biophysics and Quantitative Biology, University of Illinois at Urbana-Champaign, Urbana, IL, USA. ⁴Department of Anesthesiology, Medical College of Wisconsin, Milwaukee, WI, USA. ⁵Department of Physiology, Medical College of Wisconsin, Milwaukee, WI, USA. ⁶Cancer Center and Cardiovascular Center, Medical College of Wisconsin, Milwaukee, WI, USA. ⁷Department of Pharmacology & Toxicology, Medical College of Wisconsin, Milwaukee, WI, USA. ✉email: wmkwok@mcw.edu; emad@illinois.edu

Mitochondria are the primary source of ATP production in eukaryotic cells. Newly generated ATP is transported out of the mitochondrial matrix via the adenine nucleotide transporter at the inner mitochondrial membrane and out to the cytosol through the voltage-dependent anion channel (VDAC) located in the outer membrane of mitochondria (OMM). VDAC1, the most abundantly expressed isoform of VDAC, serves as the main conduit for the large flux of ions, ATP/ADP, metabolites, organic anions, and various respiratory substrates across the OMM^{1–3}. In addition to its function as the major gateway in and out of mitochondria, VDAC1 also acts as a scaffold, regulating mitochondrial-triggered apoptotic signaling through interactions with a variety of proteins^{2,4–6}.

VDAC1 has been reported to bind to pro- or anti-apoptotic proteins that can alter the permeability of the OMM and promote or prevent cell death^{7–15}. For example, VDAC1 serves as a receptor for the cytosolic anti-apoptotic protein hexokinase (HK) which enhances cell survival^{7,8}. Interaction with VDAC1 not only modulates cell survival but also gives HK preferential access to ATP for its catalytic activity of phosphorylating glucose to glucose-6-phosphate during glycolysis¹⁶.

HK is known as one of the primary factors of high glycolytic characteristics of rapidly growing tumor cell¹⁷. In particular, HK isoforms HKI and HKII are overexpressed in many types of cancers^{4,18–20}. Elevated levels of HKI and HKII lead to a high rate of glycolysis, known as the Warburg effect, resulting in the enhanced generation of lactic acid, a key component in promoting cell growth^{21–23}. Coincidentally, HKI and HKII both differ from other HK isoforms with one extra structural element: in addition to two homologous hexose binding domains (N-domain and C-domain, Fig. 1a), HKI and HKII have a short N-terminal hydrophobic helix (termed H-anchor hereafter, Fig. 1a) that is thought to be capable of membrane-binding²⁴. Given the importance of HK/VDAC1 interaction in cell growth and survival, disruption of this protein–protein complex has been identified as a potentially effective therapeutic strategy to prevent rapidly growing tumor cells^{25–30}.

While a number of VDAC1 residues have been identified to be essential for interaction with HKI and HKII isoforms^{7,21,31–35}, structural details of their complex remain unknown. Two protein–protein docking studies have been reported for modeling the complex formation between HK isoforms and VDAC1^{36,37}. Both studies proposed direct plugging of the H-anchors of HKI/HKII into the pore of the barrel-shaped VDAC1. However, these models failed to address several key characteristics of HK/VDAC1 interactions, e.g., how the binding of HKI only partially reduces

the maximal conductance of VDAC1^{7,21,25,31}, as the plugged model would result in a complete blockade of the channel. Furthermore, at the docked interface, there is a mismatch between the hydrophobic H-anchor from HKI or HKII and the highly charged VDAC1 interior surface (Fig. 1a, b)³⁸.

It is known that HKs can bind to membrane even in the absence of VDAC1^{39–41}, and the H-anchor is shown to be essential for this membrane interaction^{24,39,40}, likely due to its hydrophobic nature. Immunoblotting of mitochondria-bound HKI and HKII has shown that truncating the hydrophobic portions of the H-anchor disrupts HK binding to native OMM (even in the presence of VDAC1)^{42,43}. The significance of the H-anchor in OMM binding is further emphasized by the fact that HK homologs lacking the H-anchor show no mitochondrial localization^{20,44,45}. Possibly due to the inability to bind the membrane, truncation of the HKI H-anchor also eliminates the effect on the VDAC1 conductance⁷. Thus, the H-anchor in both HKI and HKII is vital for interaction with the OMM, a step that appears to be a prerequisite for the HK-induced VDAC1 blockade. Henceforward, we hypothesized the following scenario in the complex formation between HKs (HKI or HKII) and VDAC1: first, HK binds to the OMM by inserting its H-anchor, a step that aligns the H-anchor for interaction with and binding to the outer-rim of VDAC1, in order to form the complex on the cytosolic surface of the OMM (Fig. 1c).

Based on the hypothesis described above, we designed a modeling approach involving two major steps. In the first step, we describe membrane binding of HKII with molecular dynamics (MD) simulations. Next, the resulting membrane-bound HKII is used to study the formation of its complex with VDAC1 using Brownian dynamics (BD) simulations. Our results show that HKII binds to the membrane by inserting its H-anchor, independent of VDAC1. The resulting complex reveals two key functional features of HKII/VDAC1 interaction: (1) a partial, and not complete, blockage of VDAC1 conductance through HKII interaction and (2) how phosphorylation of VDAC1, and the corresponding phosphomimetic mutation, can disrupt the interaction between the two protein. Both of these predictions resulting from the computational model are supported by our designed electrophysiology measurements and mutagenesis experiments.

Results and discussion

Spontaneous membrane binding and insertion of HKII. In order to investigate direct membrane interaction of HKII, we

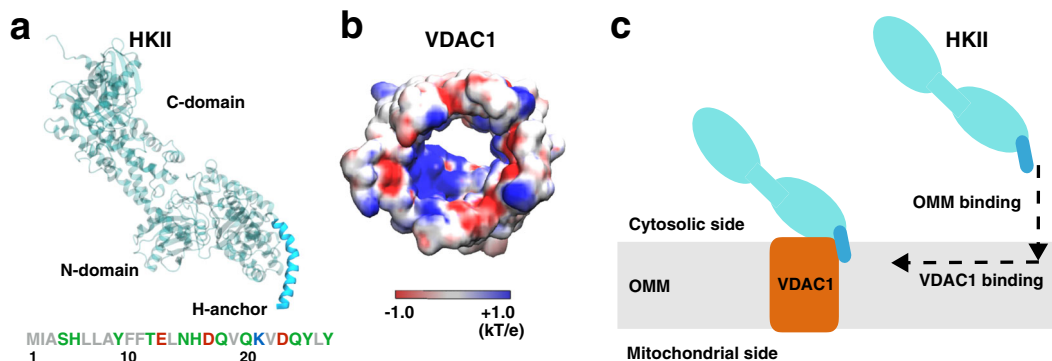


Fig. 1 HKII and VDAC1 structures and the design of our modeling approach. **a** The structure of HKII contains N- and C-domains (teal), and an N-terminal helix named here as H-anchor (cyan). The amino acid sequence of H-anchor is shown below, colored by their residue types: gray representing hydrophobic, green polar, red acidic, and blue basic amino acids. **b** The top-down view of VDAC1 colored by its electrostatic potential, generated using the Poisson–Boltzmann (PB) equation solver in CHARMM-GUI^{73,86,93}. **c** Schematic representation describing our modeling approach in which HKII binds the outer mitochondrial membrane (OMM) first, and then membrane-bound HKII forms a complex with VDAC1.

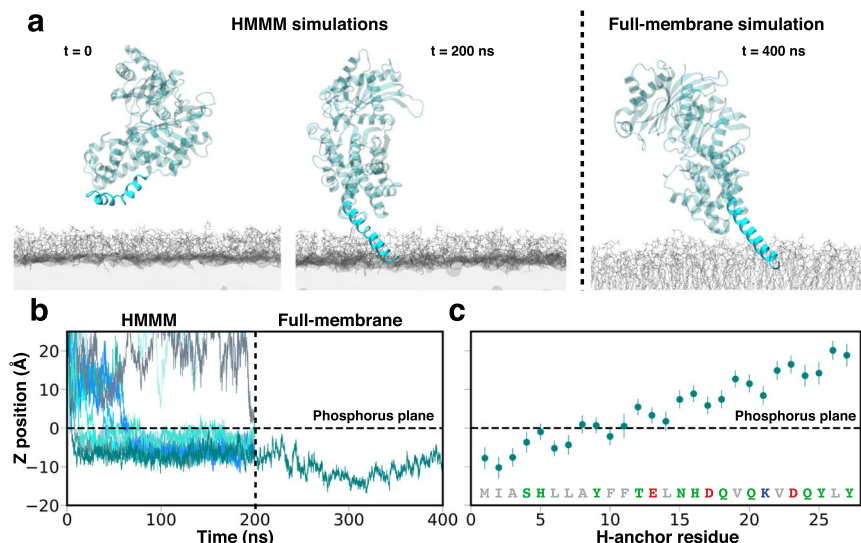


Fig. 2 Membrane binding of HKII-N. **a** Initial and final, membrane-bound configurations of HKII-N in a representative trajectory. Initial, spontaneous membrane binding simulations (200 ns each) were performed using HMMM membranes (left panel). After membrane binding was achieved, the membrane was converted to a full membrane consisting of full-tailed lipids (right panel), and the system further simulated for 200 ns (totaling 400 ns). The coloring scheme of HKII is identical to Fig. 1. Membranes are colored in gray. **b** Insertion depth of the protein into the membrane monitored by the position of I2 in HKII-N along the membrane normal (z-axis) with respect to the plane of the lipid phosphorus atoms (horizontal dashed line). The vertical dashed line separates the initial, HMMM membrane binding simulation (left side, all 12 simulation replicas shown), from the following 200-ns, full-membrane simulation performed for one of the systems (right side). **c** Mean and standard deviation of the relative z positions of the center of mass (COM) of the H-anchor residues, calculated from the last 100 ns of the full-membrane simulation.

performed 12 independent 200-ns MD simulations using the highly mobile membrane mimetic (HMMM) model⁴⁶ (Fig. 2a, more details in SI), during which binding of the N-domain of HKII (referred to as HKII-N) to lipid bilayers representing the OMM was simulated. Each simulation started with HKII-N initially placed in the solution above the membrane with a different initial orientation (Figs. 2a and S1). Binding of HKII-N to the membrane was observed in 10 out of 12 replicas (Fig. 2b), all with the H-anchor inserting into the membrane. Spontaneous membrane binding occurs within the first 50 ns of the simulations in 9 out of the 10 successful replicas. After the first encounter with the membrane, the H-anchor is rapidly inserted into the membrane and the HKII-N remains membrane-bound for the remainder of the simulation (Fig. 2b). The H-anchor reaches a maximum depth of 10 Å below the bilayer's phosphorus plane (as measured by the insertion of residue I2), penetrating well into the membrane's hydrophobic core (Fig. 2b). Membrane partitioning and orientation (with respect to the membrane normal) of the H-anchor were similar in all membrane-bound replicas (Figs. S1 and S2), suggesting convergence in the obtained membrane-bound configuration of HKII-N.

To ensure that the final membrane-bound model of HKII-N obtained from the HMMM simulations was stable, we converted one of the resulting membrane-bound systems to a conventional, full membrane and simulated it for additional 200 ns. The H-anchor remains buried into the hydrophobic core of the full membrane during the simulation (Fig. 2). In fact, the H-anchor appears to become even more engaged with the membrane during this additional stimulation, as evidenced by deeper penetration of I2 into the membrane, reaching a maximum depth of 17 Å below the phosphorus plane of the lipid head groups' approximately at $t = 300$ ns (Fig. 2b). These results provide strong support and a model for the direct interaction of HKII with the membrane. Membrane partitioning of the H-anchor obtained from the full-membrane simulation shows that the first 10 residues remain stably bound and/or insert into the membrane (below the phosphorus plane) (Fig. 2c). This finding substantiates the

experimental results where truncation of the first 10 residues from HKII was shown to disrupt its OMM binding⁴². Hence, our results provide the first structural model for membrane-bound HKII.

HKII/VDAC1 complex formation. Once we established the membrane-binding mode of HKII-N using MD simulations, we extended our study to investigate the molecular interaction between membrane-bound HKII-N with membrane-embedded VDAC1 by performing an aggregate of millisecond-scale atomic-resolution BD simulations. BD simulations were performed by placing 100 independent replicas of HKII-N around VDAC1 (Fig. 3a–c); each system was simulated for 20 μ s, totaling 2 ms. During the simulations, the membrane-bound pose of HKII-N was preserved using restraints designed based on the MD simulation results. These restraints allowed for the lateral diffusion of HKII-N around VDAC1 but prohibited significant vertical displacement of the system with respect to the membrane plane, thereby approximating the membrane-insertion depth and orientation of HKII-N (Fig. 3a, Supplementary Movie 1). Details for the BD simulations are provided in SI text.

The BD simulations revealed five distinct hot spots for HKII-N to bind VDAC1 while remaining anchored in the membrane (Fig. 3d). To further investigate whether these hot spots represent distinct HKII-N/VDAC1 complexes, we performed cluster analysis of HKII-N's relative position to VDAC1 (using C_{α} root-mean-square deviation as a reference) for BD trajectories when the two are in close contact (i.e., having at least 1 atom within 3.0 Å cutoff distance). The top five distinct clusters resulted from our analysis match the locations of the 5 BD hot spots (Fig. 3d). A representative HKII-N/VDAC1 complex, with the most favorable interaction energy between HKII-N and VDAC1, was selected for each of the five clusters (complexes termed HKV1, HKV2, HKV3, HKV4, and HKV5, respectively, for Clusters 1–5). Each HKII-N/VDAC1 complex model was then used to generate a full-length HKII/VDAC1 complex by

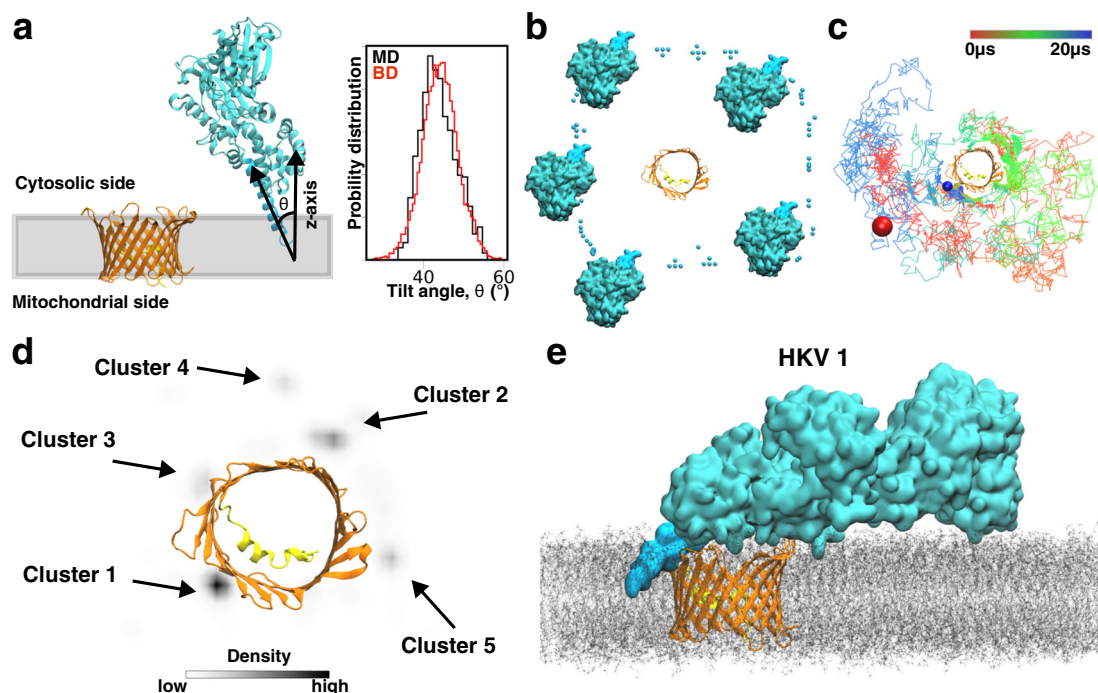


Fig. 3 Binding of membrane-inserted HKII-N to VDAC1 and their complex formation. **a** Side view of the initial configuration in a BD simulation. During the simulation, restraints along the z-axis (direction normal to the membrane plane represented as the gray box) were applied to the H-anchor, to maintain the positioning and the tilt angle distribution of the H-anchor (*Inset*) in BD simulations close to those observed in full-membrane MD simulations (see SI for more details). For tilt comparison, the distributions obtained from 1.5 μ s of ARBD simulations of HKII-N (in the absence of VDAC1) and the last 100 ns of full-membrane simulation of HKII-N are compared in the inset. VDAC1 is colored in orange with its N-terminal helix in yellow. The coloring scheme of HKII-N is identical to Fig. 1. **b** Top-down (cytosolic) view showing the initial placements of HKII-N around VDAC1 in independent BD simulations. Only 5 out of 100 HKII-N replicas are shown in full for clarity. The initial positioning of the other 95 replicas is represented by the COM of the H-anchor. **c** A representative BD simulation trajectory showing the collision and interaction of HKII-N with different locations of the outer rim of VDAC1 and its eventual binding. The colored line tracks the position of the COM of the H-anchor over a 20- μ s BD simulation. The initial and final positions of the H-anchor are shown as red and blue spheres, respectively. **d** The density map of the COM of H-anchor, calculated using the trajectories from all 100 independent BD replicates. The density map was calculated using the kernel density approximation module implemented in Seaborn⁹⁴. Five distinct density hot spots, each corresponding to a different cluster, are highlighted with black arrows. The clusters are ranked according to their population (Table S1). **e** A snapshot (at $t = 350$ ns) of membrane-embedded HKII/VDAC1 complex 1 (HKV1) during the full-membrane MD simulation.

extending the HKII C-domain from HKII-N. The resulting complexes were then inserted into a full membrane, creating five independent systems for additional MD refinement simulations (Figs. 3e and S3), during which the proteins and the membrane are allowed to relax conformationally, and the interfacial residues can adjust better to the new environment provided by binding of the partner protein. Each system was simulated in two replicates. Among the five complexes, HKV1 maintained the strongest interaction with VDAC1 during the 650 ns of MD refinement (Figs. S3 and S4, Supplementary Movies 2 and 3). In HKV2, relatively weak HKII/VDAC1 interactions were observed (Figs. S3 and S4). Furthermore, the binding mode observed in HKV2 would interfere with the dimeric interface of VDAC1⁴⁷, reducing the probability of its *in vivo* relevance (Figs. S3 and S5, Supplementary Movies 4 and 5). In contrast, the binding mode observed in HKV1 does not interfere with the proposed dimeric interface of VDAC1⁴⁷ (Fig. S5). For the rest of the complexes (HKV2, HKV3, and HKV5), either a complete dissociation or negligible HKII/VDAC1 interactions were recorded during their respective MD refinement simulations (Figs. S3 and S4, Supplementary Movies 6–11). Moreover, HKV1 corresponds to the highest population cluster (Table S1). Therefore, we consider HKV1 as the most relevant system and used it for further structural analysis.

In HKV1, multiple hydrogen bonds and salt-bridge interactions between VDAC1 and HKII (H-anchor and N-domain)

maintained the stability of the complex during the MD simulations (Fig. S6). These interactions promoted slightly deeper membrane insertion and a larger tilt angle (relative to the membrane normal) of H-anchor in HKV1 when compared to the membrane-bound configuration of HKII-N alone (Fig. S7). Though overall interactions seem to reach a steady state (Fig. S3), some individual interactions were only maintained intermittently (Fig. S6). This suggests that much longer equilibration may be needed to obtain a properly relaxed structure, as expected considering the fact that complex formation occurs on a minute time-scale (based on current, indirect experimental observation [see below]). Nevertheless, no contacts were observed between the C-domain of HKII and VDAC1 (Fig. S12). This is consistent with previous experiments where mitochondrial binding of HKII (and HKI) was observed with immunoblotting of H-anchor+N-domain, but not with the C-domain only⁴³.

HKII modulates VDAC1 conductance. Upon complex formation, HKII covers a large fraction of the cytosolic surface of VDAC1 (Fig. 4a), primarily due to the contacts from the N-domain. This coverage results in an almost halved cytoplasmic opening of VDAC1 (reduced from 13.0 to 7.3 Å, Fig. 4b), suggesting that the VDAC1 conductance might be affected upon HKII binding. To further test this hypothesis and quantify the effect, we performed constant-voltage MD simulations for both HKII-free and HKII-bound states of VDAC1. Three independent

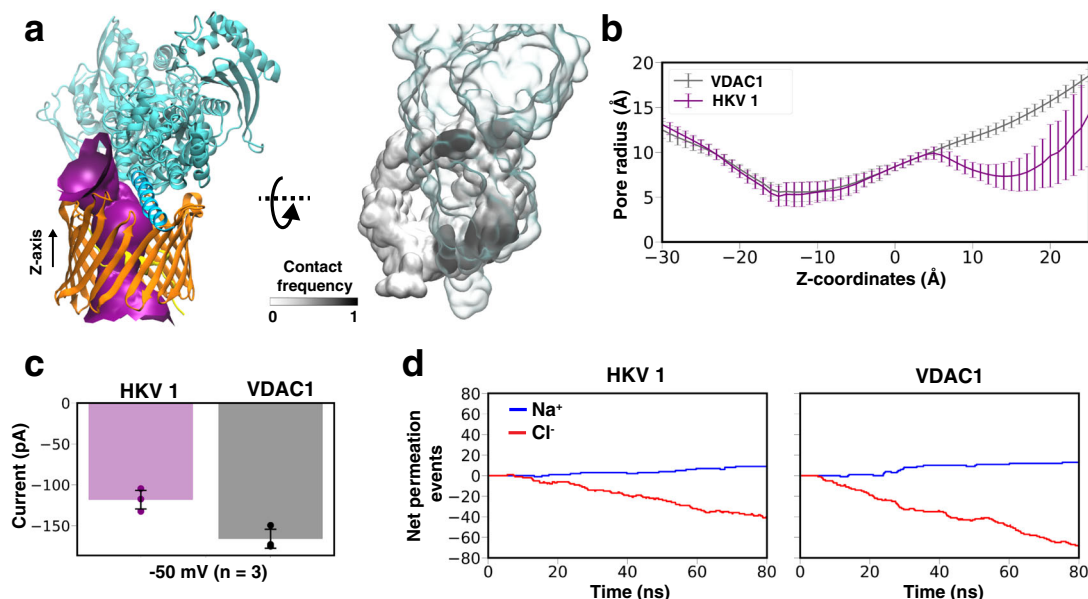


Fig. 4 HKII/VDAC1 interaction in Complex HKV1. **a** Purple surface showing VDAC1 pore radius profile in HKV1, made with the program HOLE⁹⁵ (left panel). Z-axis represents the membrane normal. (Right panel) Top-down (cytosolic) view of contact frequencies of HKII (transparent representation) mapped onto the surface of VDAC1 (black and white), calculated using the last 450 ns of MD simulation of both replicas. **b** The average radius profile of the VDAC1 pore calculated using HOLE⁹⁵ for both VDAC1 alone, and its complex with HKII (Complex HKV1). **c** The *in silico* VDAC1 current at -50 mV for a membrane-equilibrated VDAC1 alone or the VDAC1/HKII HKV1 complex calculated from electric-field MD simulations. The mean and standard deviation of current for each system were calculated from three independent simulations. **d** The cumulative net number of channel-crossing events by Cl^- (red traces) and Na^+ (blue traces), tracked over the time course of a representative MD simulation for VDAC1 or the HKV1 complex.

simulations were performed for both states, each under a -50 mV membrane potential for 80 ns. Ionic currents obtained from these simulations showed that VDAC1 conductance is indeed partially reduced upon HKII binding (Fig. 4c, d), agreeing with previous electrophysiology measurements of HKI-bound VDAC showing partially reduced channel conductance^{7,21,31}. On the other hand, the H-anchor plugged model proposed in previous computational studies^{36,37} would virtually block the channel permeability completely, as indicated by the drastic narrowing of the pore to a 2.1 Å effective radius and a negligible current in constant-voltage simulations (Fig. S13), which cannot account for the partial reduction of current observed experimentally upon HKII/VDAC binding.

The hallmarked partial blockage of VDAC1 current upon HKII binding demonstrated in the simulations was further corroborated with a series of electrophysiology measurements. Using the planar lipid bilayer method previously described⁴⁸, the reconstitution of wild-type (wt) VDAC1 and its insertion into the bilayer was evidenced by its unique voltage-dependent gating characteristic in response to a voltage ramp protocol from -80 to $+80$ mV, where the maximal conductance occurs approximately between -50 and $+50$ mV and lower conductances at the more hyperpolarizing or depolarizing potentials (Fig. 5a). After washing away the remaining soluble VDAC1, the current was monitored under a -30 mV test potential for 30 s at 2 min intervals. When HKII was added to the *cis* chamber of the planar lipid bilayer (corresponding to the cytosolic side), there was a marked decrease in the maximal conductance of VDAC1 (Figs. 5b, S14). Steady-state levels were reached in ~ 6 min, and this latency may be due to the time it takes for the membrane insertion of HKII and its diffusion at the bilayer before reaching VDAC1. Upon reaching a steady state, the effect of HKII on VDAC1 was stable for the subsequent 18 min of experiment time. Note that the addition of HKII resulted in only the reduction of VDAC1 conductance but not a complete blockade. These results strongly support the HKV1 model in MD simulations (Fig. 4)

where the N-domain of HKII only partially covers the permeation pathway of VDAC1 and partially reduces the conductance.

Phosphorylation of VDAC1 disrupts HKII binding. The immense HKII/VDAC1 interaction energy shown in MD simulations (Figs. S3 and S4) and the composition of the HKII/VDAC1-binding interface (Fig. S6) strongly suggest the binding interactions between HKII and VDAC1 are dominated by salt bridges. Therefore, their complex formation might be interfered or disrupted with the presence of additional charged species, such as post-translational modifications to the proteins. Coincidentally, an earlier proteomics screening of phosphorylated mitochondrial proteins has identified S215 of VDAC as a phosphorylation site *in vivo*⁴⁹, which is located at the HKII/VDAC1 binding interface (Fig. S6).

To investigate the impact of S215 phosphorylation on complex formation between HKII and VDAC1, we repeated the BD simulations after introducing a phosphoserine residue at position 215. Whereas BD simulation of wt-VDAC1 resulted in an HKII-binding hot spot near S215 (Cluster 1), the probability of HKII presence at this region is substantially reduced after S215 phosphorylation (Fig. 6b), suggesting that the formation of HKII/VDAC1 complex can be inhibited when S215 is phosphorylated. The disappearing of population corresponding to Cluster 1 can also be predicted by the greatly reduced HKII/VDAC1 interaction energy if a phosphoserine is directly placed at S215 position of the BD trajectories of wt-VDAC1: the electrostatic interactions between the two proteins suffered from ~ 2.6 -fold reduction on average in Cluster 1, while other clusters showed only minor changes (Fig. S15).

VDAC1 phosphorylation is known to modulate HKII binding *in vivo*⁴⁰. Therefore, the impact of VDAC1 S215 phosphorylation to HKII/VDAC1 interactions was further corroborated with an electrophysiology experiment using a phosphomimetic mutant of VDAC1, S215E. Comparing to wt-VDAC1, the HKII-induced

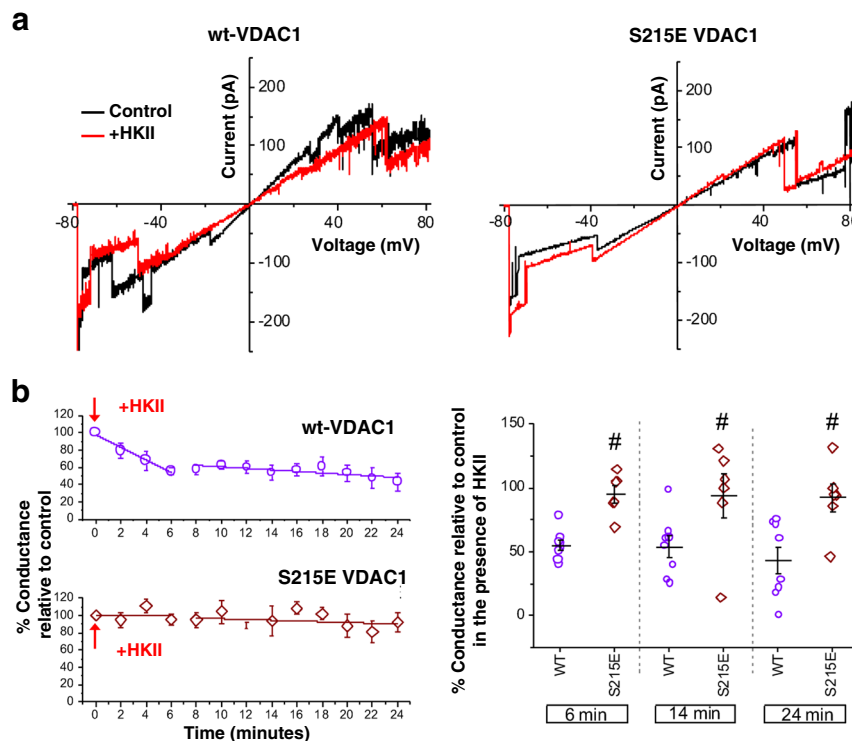


Fig. 5 Effects of HKII on wt-VDAC1 and S215E phosphomimetic mutant. **a** Current–voltage relationships for wt-VDAC1 (left) and S215E VDAC1 (right) in the absence (control; black lines) or the presence of HKII (+HKII; red lines), acquired during a -80 to $+80$ mV linear voltage ramp protocol. **b** Effects of HKII on VDAC1 conductance monitored over time (purple circles: wt-VDAC1; brown diamonds: S215E phosphomimetic mutant). Change in conductance in the presence of HKII was relative to that prior to the addition of HKII. Summary graphs are shown for both wt-VDAC1 ($n = 8$) and S215E VDAC1 ($n = 6$) in the presence of HKII. Representative steady-state current recordings for both wt-VDAC1 and S215E VDAC1 in the presence and absence of HKII are shown in Fig. S14.

partial blockage is rarely observed, if not completely abolished, in membranes containing the S215E phosphomimetic mutant of VDAC1 (Figs. 5b and S14). Additionally, the presence of HKII does not alter the current–voltage characteristics of S215E-VDAC1 significantly (Fig. 5a). Based on these observations, the S215E point mutation appeared to prevent or diminish the interaction of HKII with VDAC1, supporting the predicted outcome of the computational model.

To date, it remains unclear which kinase or signaling pathway mediates VDAC1’s phosphorylation at S215 position. We used the peptide sequence near S215 for kinase substrate prediction and did not yield a convincing kinase hit. However, since HKII/VDAC1 binding can be inhibited by the S215 phosphorylation, the kinase responsible for S215 phosphorylation is expected to belong to a pro-apoptotic pathway or at least not in a pathway promoting cell survival. Intriguingly, VDAC1 is a known substrate of glycogen synthase kinase (GSK)-3 β ³⁵, a major promoter of mitochondrial intrinsic apoptotic pathway⁵⁰. VDAC phosphorylation by GSK3 β is also linked to a reduced HKII binding³⁵, and the disruption of HK binding to VDAC1 has been shown to play an essential role in several diseases including cardiac ischemia-reperfusion injury^{51–53}, by promoting mitochondria-mediated cell death^{7,35,54}. The matching phenotype leads us to speculate that the kinase responsible for VDAC1 S215 phosphorylation might be GSK3 β .

GSK3 β is known to highly favor a “primed” substrate where another phosphorylated serine/threonine is located at the $+4$ residue position downstream of the phosphorylation site⁵⁵. One may argue that in VDAC1, such position is a membrane-embedded F219, which cannot be phosphorylated and serve as a priming residue for GSK3 β recognition (Fig. 6a). Based on crystal

structures of GSK3 β with a bound pseudo-substrate phosphopeptide inhibitor⁵⁶, GSK3 β seems to recognize substrate peptides with an extended backbone configuration where the priming phosphate sits ~ 13 Å away from the transferring γ -phosphate. Interestingly, the β -barrel VDAC is full of extended backbones and its cytoplasmic rim has a number of serine and threonine residues, among them S215 is located at a β -turn slightly protruding out of the membrane surface and is exposed to the cytosol (Fig. 6a). In addition, residue S240 is located at the immediately following β -turn at the cytoplasmic side and is in line with the downstream residues of S215, spacing on average 14.3 ± 1.7 Å between the two hydroxyl groups in our simulations (Fig. 6a). Most importantly, S240 was also found phosphorylated *in vivo* in the mitochondrial proteomics study⁴⁹. The proximity of phospho-S240 from S215 and the extended backbone configuration of residues between them make it possible for GSK3 β to bind to the cytoplasmic rim of VDAC1, recognizing phospho-S240 and phosphorylating S215.

Although the consensus sequence of GSK3 β substrate peptides S/T-X-X-X-S/T(P)⁵⁷ would predict subsequent T211 phosphorylation if S215 is phosphorylated by GSK3 β , the two residues are situated right at the two ends of the same β -turn (Fig. 6b). It is therefore unlikely that phospho-S215 can be the primer for GSK3 β to phosphorylate T211 of VDAC1 due to incompatible backbone configuration. To date, we have yet to discover a literature reporting T211 phosphorylation of VDAC.

Other VDAC1 residues implicated experimentally in complex formation with HK. Several other VDAC1 residues have been previously identified as essential for interaction with HKI and

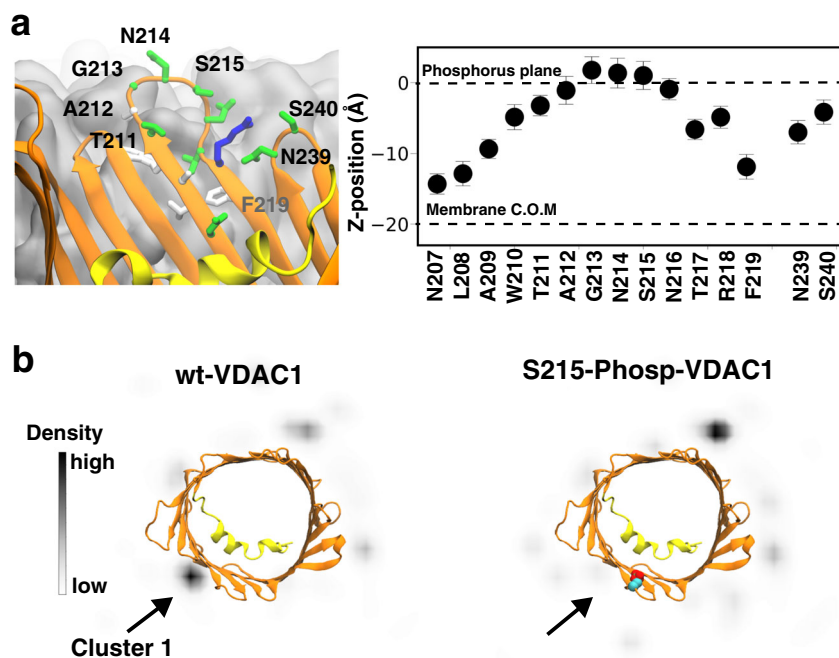


Fig. 6 Phosphorylation of S215 in VDAC1 disrupts HKII/VDAC1 binding. **a** Cytosolic accessibility of S215. VDAC1 barrel viewed from the membrane plane, highlighting the position of S215 at a location accessible to bulk solvent (left panel). The membrane is colored in gray. (Right panel) Mean and standard deviation of the relative positions along the membrane normal (z-position) of the COM of the side-chain of highlighted VDAC1 residues (light), derived from a 200-ns MD simulation of membrane-embedded VDAC1. **b** Top-down (cytosolic) view of the xy projection of densities of the COM of the H-anchor bound to VDAC1 during the BD simulations. The densities are obtained using all 100 independent replicates of the BD simulations for wt-VDAC1 (left) and S215-phosphorylated (S215-Phosp-VDAC1, right).

HKII isoforms^{7,21,31–35}. To examine if our modeled complexes provided any evidence in support of the role for these interactions, we analyzed all possible hydrogen-bond and salt-bridge interactions between VDAC1 and HKII formed at any point during the MD simulations of all five complexes (Figs. S6 and S8–S11). We captured several interaction pairs which involve previously identified VDAC1 residues: E189(VDAC1)–R373(HKII) in HKV1 (Fig. S6), D78(VDAC1)–K346(HKII) in HKV2 (Fig. S8), and D78(VDAC1)–K323(HKII) and T51(VDAC1)–E317(HKII) in HKV3 (Fig. S9). E189Q and D78N mutations (independently) of VDAC1 have been reported to inhibit the protective effect of HKI overexpression against apoptotic cell death^{21,32}. According to our simulations, these mutations might interfere with the complex formation between VDAC1 and HK, for example, by disrupting the interaction of E189(VDAC1) with H373 of HKI, which is likely protonated, or with R373 of HKII. Other interactions affected by these mutations include D78–K346 (K346 is conserved between HKI and HKII) or D78–R323 (K323 of HKII is replaced by an R323 in HKI) bonds. Phosphorylation of VDAC1 at residue T51 by GSK3 β has been previously shown to dissociate HKII from the mitochondria³⁵. This phosphorylation might destabilize the HKII/VDAC1 complex by disrupting the T51(VDAC1)–E317(HKII) bond due to the electronegative group introduced at T51. The involvement of several other VDAC1 residues in direct interactions with HKII (or HKI) cannot be explained by our modeled complexes. One possible explanation is that these mutations do not disrupt the complex formation by direct inhibition of HK/VDAC1 interactions, rather, through other cellular processes such as VDAC1 oligomerization.

Higher-order HKII and VDAC1 organization. While in this study, we have focused on the complex formation between one

VDAC1 and one HKII, reportedly they can also form higher-order organizations. HKII has been reported to exist as a monomer or a tetramer; intriguingly, no intermediates, i.e. dimers and trimers, have been detected^{58,59}. The mechanism underlying the formation of tetramers and their exact arrangement are not known. It has been speculated that an initial translocation of an HKII monomer to the OMM may encourage the binding of subsequent HKII monomers to form a tetrameric complex around VDAC1. Confounding the interaction between VDAC1 and a tetrameric complex of HKII is that VDAC1 itself may also oligomerize^{60,61}. VDAC1 has been reported to exist as monomers, dimers, trimers, tetramers, and even hexamers^{60,61}. Though a tetrameric HKII is speculated to interact with VDAC1 oligomers, the stoichiometry of interactions between HKII tetramers and VDAC1 monomers/oligomers remains unknown. It should also be noted that while translocation of HKII is associated with cell survival, oligomerization of VDAC1 can result in apoptosis². Thus, the dynamic process regulating the interaction of tetrameric HKII with oligomeric VDAC1 still needs to be delineated. Nevertheless, our computational model presents the first steps in the translocation and binding of monomeric HKII to the OMM and its interaction with VDAC1.

Concluding remarks

Atomic structures of protein complexes are usually derived from experimental techniques such as X-ray crystallography and cryo-EM. In the case of HKII/VDAC1 complex formation, a priori requirement of membrane binding of HKII hinders structural determination in typical experimental techniques. Simulation of this process is also challenging because complex formation occurs on a time-scale (in the order of minutes based on current, indirect experimental observation [Fig. 5b]) not feasibly obtained by conventional or enhanced sampling MD simulation techniques.

Therefore, we designed a hybrid modeling approach integrating MD and BD simulations and report a stable structural model for the HKII/VDAC1 complex, which we validated using complementary experiments at multiple levels. The complex partially blocks the permeation pathways of the VDAC1 channel, a key feature that was also observed in our electrophysiology measurement, strongly supporting the relevance of the derived complex structure. Furthermore, the binding interface of the complex is highlighted by the presence of a potential phosphorylation site S215, whose phosphorylation/phosphomimetic mutation results in inhibition of HKII/VDAC1 interactions both in our BD simulations and in our electrophysiology recordings. This inhibition appears to be mediated through disruption of the electrostatic attraction between H-anchor and cytosolic outer-rim of VDAC1.

Though other phosphorylation sites on VDAC1 have been identified^{2,52} and several of these sites have been implicated in cardiac and neurodegenerative diseases, their functional consequences have not been delineated. Our study shows that phosphorylation of a single residue, S215, can disrupt HKII interaction with VDAC1. This provides insight into how phosphorylation of specific sites on VDAC1 can impact its binding with HKII and potentially other proteins that translocate to mitochondria, for example, the pro-apoptotic protein BAX. Characterizing the complex molecular interactions between VDAC1 and anti-apoptotic and pro-apoptotic proteins will help delineate their roles in cell death and survival.

Methods

Membrane binding simulations. We used the X-ray structure of human HKII (PDB ID: 2NZT) as a starting point for our simulations. Glucose and glucose-6-phosphate were removed from the crystal structure, and one monomer from the HKII dimer was selected for the simulations. The missing regions (residues 1–16, 98–104, 346, 404–405, 518–525, 546–552, 645–649, 914–917) from the crystal structure were modeled using MODELLER⁶². Among missing regions, residues 1–16 were predicted to be in an α -helical structure by the secondary structure prediction tool YASPIN⁶³, while other missing regions were predicted to be unstructured. As residues 1–16 are a part of the H-anchor and known to be crucial for membrane-binding, we carefully modeled this part by using as a template the highly homologous isoform enzyme from rat, HKI (PDB ID: 1BG3), for which the H-anchor is fully resolved as an α -helix. Notably, the H-anchor of rat HKI shares high sequence similarity with human HKII (Fig. S16). Other missing regions were modeled as loops using conjugate gradients and MD with a simulated annealing approach in MODELLER⁶⁴.

To reduce the system size in our membrane-binding simulations, we removed the C-domain and used only the N-domain (residues 1–463) of human HKII for membrane binding simulations. N-domain of human HKII, referred to as HKII-N hereafter is known to be sufficient for binding to the OMM⁴³. In order to assign the protonation states of ionizable residues of HKII-N, pK_a values were estimated using PROPKA^{65,66}. Then, HKII-N was placed above a symmetric HMMM lipid bilayer composed of 108 phosphatidylcholines (PC), 58 phosphoethanolamines (PE), 26 phosphatidylinositols (PI), 4 phosphatidylserines (PS), and 2 phosphatidic acids (PA) lipid molecules in each leaflet. The lipid composition was chosen to approximately replicate the OMM of mammalian cells⁶⁷. HKII-N was placed 5 Å above the membrane, where 5 Å is the minimum distance between any HKII-N atom and any membrane atom along the membrane normal (z -axis). Twelve independent HMMM systems were constructed using CHARMM-GUI⁶⁸, each resulting in a box with dimensions of $125 \times 125 \times 174 \text{ \AA}^3$, including 240,000 atoms. To minimize possible bias in membrane binding simulations due to a particular initial lipid distribution, the lipid bilayers in all replicas were generated independently using CHARMM-GUI⁶⁸ to obtain a different (randomized) initial lipid distribution for each replica. All replicas were neutralized with 150 mM NaCl and solvated with the TIP3 water⁶⁹. All the 12 solvated HMMM systems were then energy-minimized for 2500 steps before used for the subsequent 200 ns membrane binding simulations. A harmonic restraint on the z -position (along the membrane normal) was applied to the carbonyl atoms of short-tailed lipids with a force constant of $k = 0.1 \text{ kcal mol}^{-1} \text{ \AA}^{-2}$, to mimic the atomic distributions of a full-tailed lipid bilayer and to prevent occasional diffusion into the aqueous phase^{70,71}.

Conversion of HMMM lipids to full-tailed lipids. In order to generate a complete model of membrane-bound HKII-N, we used the last frame of one of the HMMM membrane-binding simulations described above and converted it to a full-membrane construct using CHARMM-GUI⁶⁸. Short-tailed HMMM lipids were transformed into full lipids by removing the DCLE molecules and adding the

missing carbons to the lipid tails while preserving the positions of the headgroups and the initial six carbons of the lipid tails. The system was then energy-minimized for 10,000 steps and then equilibrated for 2 ns, while harmonic restraints (force constant, $k = 1 \text{ kcal mol}^{-1} \text{ \AA}^{-2}$) were applied to (1) the heavy atoms of the protein and (2) the positions of lipid heavy atoms corresponding to short-tailed lipids only in the *cis* leaflet of the lipid bilayer (the leaflet facing the protein). These restraints were applied to preserve lipid-protein interactions established during the association of the protein with the lipid membrane in HMMM simulations, while the newly added carbon atoms adjusted to the system⁷². Following this step, the system was simulated without restraints for 200 ns, resulting in a fully relaxed, membrane-bound protein.

Simulation of membrane-embedded VDAC1. The X-ray structure of mouse VDAC1 (PDB ID: 3EMN)³⁸ was embedded in a full membrane, with the same lipid composition as described above, using CHARMM-GUI⁷³. Mouse and human VDAC1 proteins have a sequence identity of 94%. The system was neutralized with 150 mM NaCl and solvated with TIP3 water⁶⁹ resulting in a box size of $120 \times 120 \times 84 \text{ \AA}^3$ including 110,000 atoms. Then the system was energy-minimized for 2500 steps and equilibrated for 1 ns, during which $C\alpha$ atoms of the protein were harmonically restrained with a force constant $k = 1 \text{ kcal mol}^{-1} \text{ \AA}^{-2}$. Following this step, the system was simulated without restraints for 200 ns.

MD simulation of HKII/VDAC1 complexes. For each of the complexes (HKV1, HKV2, HKV3, HKV4, and HKV5) derived from the BD simulations, a full-length HKII/VDAC1 model was generated by adding the C-domain of HKII to the coordinates of the HKII-N/VDAC1 complex (based on the known full structure of HKII). Each extension was carried out by adopting coordinates from full-length HKII after superimposing the backbone atoms of residues S449-L463 (an α -helix) into HKII-N. The resulting full-length models were then embedded in a full-membrane with the same lipid composition as described above using CHARMM-GUI⁷³. These five different systems were neutralized with 150 mM NaCl and solvated with TIP3 water⁶⁹. HKV1 simulation system resulted in a box size of $215 \times 215 \times 160 \text{ \AA}^3$ including 700,000 atoms; HKV2 system resulted in a box size of $120 \times 120 \times 240 \text{ \AA}^3$ including 330,000 atoms; HKV3 system resulted in a box size of $160 \times 180 \times 140 \text{ \AA}^3$ including 330,000 atoms; HKV4 system resulted in a box size of $120 \times 120 \times 230 \text{ \AA}^3$ including 320,000 atoms; and HKV5 system resulted in a box size of $120 \times 120 \times 200 \text{ \AA}^3$ including 300,000 atoms. Two independent replicas were created for each of the systems, resulting in a total of 10 independent simulation systems. Each system was energy minimized for 2500 steps and equilibrated for 1 ns while harmonically restraining the $C\alpha$ atoms of both proteins with a force constant $k = 1 \text{ kcal mol}^{-1} \text{ \AA}^{-2}$. Each system was then simulated for 650 ns, without restraints.

MD simulation protocols. MD simulations in this study were performed using NAMD 2.13^{74,75} utilizing CHARMM36m⁷⁶ and CHARMM36⁷⁷ force field parameters for proteins and lipids, respectively. Bonded and short-range nonbonded interactions were calculated every 2 fs, and periodic boundary conditions were employed in all three dimensions. The particle mesh Ewald (PME) method⁷⁸ was used to calculate long-range electrostatic interactions every 4 fs with a grid density of 1 \AA^{-3} . A force-based smoothing function was employed for pairwise nonbonded interactions at a distance of 10 Å with a cutoff of 12 Å. Pairs of atoms whose interactions were evaluated were searched and updated every 20 fs. A cutoff (13.5 Å) slightly longer than the nonbonded cutoff was applied to search for the interacting atom pairs. Constant pressure was maintained at a target of 1 atm using the Nosé-Hoover Langevin piston method^{79,80}. Langevin dynamics maintained a constant temperature of 310 K with a damping coefficient, γ , of 0.5 ps^{-1} applied to all atoms. HMMM simulations were performed by employing a constant area in the XY dimension (membrane plane). For the full-membrane simulations, a constant ratio was used instead, which keeps the X:Y ratio of the unit cell constant. Simulation trajectories were collected every 10 ps.

Electric field simulations. Ionic current through VDAC1 was calculated by performing simulations of the membrane-embedded form of the channel in the presence of a constant electric field normal to the membrane. Simulations were performed for both HKII-free and HKII-bound states (HKV1) of VDAC1. The starting point for each simulation was the last snapshot of their respective full-membrane equilibrium MD simulation. For each system, the salt concentration was increased from 150 to 500 mM by using the AUTOIONIZE plugin of VMD⁸¹, in order to enhance the number of ion permeation events during the electric field simulations. Three independent simulations were performed for each system, under a membrane potential difference of -50 mV , each for 80 ns.

Ionic current (I) was computed by counting the number of ions (Na^+ and Cl^-) that cross the VDAC1 channel (moving all the way from one side of the membrane to the other) over time, i.e. $I = N \times \frac{q}{\tau}$, where N is the number of crossing events over a time interval τ , and q is the charge of the ion ($1.60217662 \times 10^{-19}$ Coulombs for Na^+ and $-1.60217662 \times 10^{-19}$ Coulombs for Cl^-).

BD simulation setup. We used the membrane-bound HKII-N and membrane-embedded VDAC1 to simulate the formation of their complexes using BD simulations. Atomic coordinates of both proteins were extracted from the final snapshot of their respective MD simulations in full-membranes. During the BD simulations, membrane-bound HKII-N was considered as the moving protein, while VDAC1 was the stationary protein, with both proteins modeled as rigid body entities.

Given the rigid representation of the molecular entities in BD simulations, we did not use an explicit membrane in these simulations. In order to take into account membrane placement of HKII-N and VDAC1 (as observed in the MD simulations of the membrane-bound forms of these proteins), in the beginning of each simulation, the *z*-coordinates of each protein were shifted so that their respective membrane midplanes would match (Fig. 3A). Another set of restraints were then used to maintain both the insertion position and orientation of HKII-N during the BD simulation; we applied restraints on the positions of H-anchor residues along the *z*-axis in our BD simulations. Restraints were applied on four residues (M1, F10, N15, Q20) of H-anchor using a grid-based potential coupled to each residue. Grid-based potentials were obtained by Boltzmann inversion of the probability distribution function of the *z*-coordinate of each residue obtained from the last 100 ns of membrane-bound MD simulation of HKII-N in full-membranes. Applied restraints were able to maintain the positioning and the tilt angle distribution of the H-anchor in BD simulations close to those observed in full-membrane MD simulations (Fig. 3A) while allowing for the lateral diffusion of HKII-N around VDAC1 and their complex formation. To avoid unnecessary sampling of HKII-N during simulation, we employed a circular grid-based potential wall around VDAC1 with a radius of 150 Å.

It is important to note that BD simulations do not allow for internal relaxation of the interacting proteins and the membrane upon their interaction and binding. Therefore, BD here is used to only generate an initial, unrefined candidate structure for the complex purely based on their overall (global) attraction as rigid bodies. These BD-generated structures are then subjected to several hundreds of nanoseconds of MD simulations (details in the “MD simulation of HKII/VDAC1 complexes” section) during which the proteins and their embedding membrane are allowed to relax and detailed interfacial interactions can be refined.

BD simulation protocols. BD simulations were performed using a GPU accelerated BD code, ATOMIC RESOLUTION BROWNIAN DYNAMICS (ARBD)⁸². The masses and moments of inertia of the HKII-N (moving protein) were calculated directly from its atomic coordinates. HYDROPRO program suite⁸³ was used to estimate the translational and rotational friction coefficients of HKII-N protein which provided Langevin forces and torques at each timestep to keep the system at 310 K. To be noted, our calculated friction coefficients represent the diffusive behavior of HKII-N in aqueous solutions. Though this diffusive property would be significantly different for membrane-bound HKII-N, it will not affect the results of our study, as we are not focusing on either diffusive or kinetic properties of HKII-N binding to VDAC1.

The force and torque acting on HKII-N, due to stationary protein VDAC1, were calculated as follows. First, a grid of electric charge and Lennard-Jones (LJ) particle densities were obtained from the atomic coordinates of membrane-bound HKII-N with a 1 Å resolution. The density in each grid cell experienced a local force due to the corresponding grid-specified stationary VDAC1 potential (electrostatic or LJ terms). These local forces and the corresponding torques were summed over to obtain the total force and torque on the HKII-N molecule. A cutoff of 34 Å was used for the force calculation. Electric charge and LJ particle density of the atoms comprising HKII-N were calculated using the VOLMAP utility in VMD. On the other hand, stationary protein VDAC1 was represented by the electrostatic and LJ potential map of its atomic coordinates. The electrostatic potential map for the stationary protein (VDAC1) was calculated by solving the nonlinear Poisson-Boltzmann equation implemented in the APBS software^{84,85}. *cglen* and *fglen* options in APBS were chosen to ensure a resolution of 1 Å for computing the cubic electrostatic potential grids. Dielectric constants for the protein interior and solvent were set to 12.0 and 78.0, respectively. Ionic radii were set as per the CHARMM36 force field⁷⁶. A cubic-spline surface⁸⁶ model was implemented to model the dielectric interface and ion accessibility. The rate of dielectric transition was set to 0.3 and surface density to 10. The radius of the solvent molecule was set to 1.4 Å, the same as water. These parameters are comparable to previous studies of protein-protein interactions using ARBD simulations⁸⁷.

The LJ parameters of the atoms comprising the stationary protein (VDAC1) were clustered into three categories: one representing all hydrogen atoms, another representing oxygen, and nitrogen atoms, and the final one representing carbon and sulfur atoms. The atoms in each category were assigned an average value for the parameters R_{\min} and ϵ . Then, ϵ was scaled down by 0.3, following a similar approach adopted by McGuffee et al.⁸⁸ to avoid the stickiness of proteins during the BD simulations. These two parameters, R_{\min} and scaled ϵ , were used to generate potential maps for the interaction of the three above-mentioned atom categories with the stationary protein, VDAC1, using the IMPLICIT LIGAND SAMPLING (ILS) implementation of VMD at 1 Å resolution^{81,89}. ARBD simulations were performed using a timestep of 200 fs. Simulation coordinates were collected every 0.2 ns.

Generation of an H-anchor plugged model. An alternative model for the HK/VDAC1 complex has been reported in the literature^{36,37}. In this model, which we

refer to as the “H-anchor plugged model”, the H-anchor completely plugs the VDAC1 pore. To investigate the electrophysiological properties of such a model and how VDAC1 permeability is affected, we generated an approximate model of the H-anchor-plugged HKII/VDAC1 complex by docking the H-anchor into the lumen of VDAC1, which was then used in our electric field simulation for current measurements. Docking was performed using the “easy interface” implemented in HADDOCK2.2 web portal⁹⁰. The X-ray structure of human HKII (PDB ID: 2NZT, missing regions modeled) and the same of mouse VDAC1 (PDB ID: 3EMN)³⁸ were used for docking. Docking was performed between the residues of H-anchor and the residues of VDAC1 facing the lumen on the cytoplasmic half resulting in multiple structural models. A representative structure was selected based on the best HADDOCK score, which was then embedded in a full-membrane with the same lipid composition as those used for our own model (described above) using CHARMM-GUI⁷³. The system was neutralized with 150 mM of NaCl and solvated with TIP3 water⁶⁹, resulting in a box size of $120 \times 120 \times 200 \text{ \AA}^3$ including 270,000 atoms. The newly generated system was energy minimized for 2500 steps and equilibrated for 1 ns while harmonically restraining the $\text{C}\alpha$ atoms of both proteins with a force constant of $k = 1 \text{ kcal mol}^{-1} \text{ \AA}^{-2}$. Then, the system was simulated without restraints for 100 ns before using it for computational electrophysiological measurements.

Analysis. System visualization and analysis were carried out using VMD⁸¹. Depth of insertion of HKII-N into the membrane was assessed by calculating the *z* component of the center of mass (COM) of protein side-chain atoms relative to the average plane of the phosphorous atoms of the membrane. Interaction energy (van der Waals + electrostatic) between HKII-N and VDAC1 was calculated using the NAMDENEGY plugin of VMD. Contacts between HKII and VDAC1 are calculated using a 3 Å distance cutoff between any atoms of the two proteins. A hydrogen bond was counted to be formed between an electronegative atom with a hydrogen atom (H) covalently bound to it (the donor, D), and another electronegative atom (the acceptor, A), provided that the distance D–A is $< 3 \text{ \AA}$ and the angle D–H–A is more than 120° . Clustering was performed based on the position of the HKII-N with respect to VDAC1 (calculated using the root-mean-square deviation (RMSD) of HKII-N after superpositioning the BD trajectories using VDAC1). The “measure cluster” module implemented in VMD^{81,91} was used for clustering analysis with an RMSD cutoff of 10 Å.

Generation of VDAC1 mutant construct. Full-length cDNA of rat VDAC1 (GenBank: BC072484, purchased from Open Biosystems) was first subcloned into pET21a vector (Novagen) to generate pET-VDAC1 (wt). The VDAC1 mutations at serine 215 to glutamate (S215E) was generated by PCR with QuikChange site-directed mutagenesis kit (Agilent Technology) using pET-VDAC1 as cDNA templates and the following primers: S215A: Forward 5'-CTC GCC TGG ACC GCA GGA AAC GCT AAC ACT CGC TTT GG-3' and Reverse 5'-C AAA GCG AGT GTT AGC GTT TCC TGC GGT CCA GGC GAG-3'; S215E Forward: 5'-CTC GCC TGG ACC GCA GGA AAC GAG AAC ACT CGC TTT GG-3' and Reverse 5'-C AAA GCG AGT GTT CTC GTT TCC TGC GGT CCA GGC GAG-3'. The plasmids pET-VDAC1, pET-VDAC1-S215A, and pET-VDAC1-S215E were separately transformed into BL21 *E. coli* for protein expression. Cells were grown at 37 °C in LB medium to A600 = 0.6 and VDAC1 protein expression was induced with 1 mM IPTG overnight. After induction, VDAC1 proteins were extracted with BugBuster Master Mix (Novagen) and purified with Ni-NTA His · Bind Resins (Novagen). Purified VDAC1 was refolded at 4 °C by slowly dropwise dilution of one volume protein into 10 volumes refolding buffer containing 20 mM Tris-Cl, 100 mM NaCl, 1% lauryldimethylamineoxide (LDAO), and 1 mM DTT at pH 7.4 with slowly stirring. The refolded VDAC1 protein was dialyzed against modified refolding buffer (0.1% LDAO and without DTT) at 4 °C to decrease LDAO concentration and to remove DTT.

Experimental electrophysiology. Recombinant rat wild-type (wt) or mutant (S215E) VDAC1 proteins were reconstituted into planar lipid bilayers as described previously⁴⁸ with some modifications. Briefly, phosphatidylethanolamine (PE) and phosphatidylcholine (PC) (Avanti Polar Lipids) were mixed in a ratio of 7:3 (v/v), dried under nitrogen gas, and resuspended in *n*-decane (Sigma) for a final lipid concentration of 25 mg/ml. The *cis/trans* chambers contained symmetrical solutions of 10 mM Trizma base (Sigma), 500 mM KCl (Sigma), and 1 mM CaCl_2 (Sigma), pH 7.4. The *cis* chamber was held at virtual ground and the *trans* chamber was held at the command voltage. The pClamp software (version 10, Molecular Devices, San Jose, CA) was used for data acquisition. Currents were digitized at 5 kHz and low-pass filtered at 1 kHz using a voltage clamp amplifier (Axopatch 200B, Molecular Devices) via a digitizer (DigiData 1440A, Molecular Devices). The recombinant VDAC1 proteins were added into the *cis* chamber. Insertion of VDAC1 into the bilayer membrane and its function was monitored and confirmed by current recordings in response to a ramp protocol from -80 to $+80$ mV, as VDAC1 is characterized by its uniquely distinct current-voltage relationship. Subsequently, the solution in the *cis* chamber was replaced with the same initial buffer solution at the speed of 2.5 ml/min to remove non-inserted VDAC1 proteins and prevent additional VDAC1 insertion into the bilayer membrane. Current recordings under control conditions (in the absence of HKII) were initially taken,

followed by addition of HKII (human recombinant HKII, 60 kU/ml; Genway Biotech, San Diego, CA) into the *cis* chamber. Currents were monitored during a 30-s recording duration every 2 min up to 24 min, and analyzed using CLAMPFIT (Molecular Devices) and ORIGIN (version 10; OriginLab, Northampton, MA). Mean current from each time point was normalized to its control as a percentage data, which was used for statistics later.

Significant differences between groups were determined with one-way ANOVA (SPSS Statistics 24, IBM) with posthoc significance analysis. $P < 0.05$ was considered significantly different.

Statistics and reproducibility. The data plotted in Figs. 2c, 3a, and 6b are the mean and standard deviation from more than 100 snapshots extracted from trajectories.

Reporting summary. Further information on research design is available in the Nature Research Reporting Summary linked to this article.

Data availability

The data that support the findings of this study are available from the corresponding author upon reasonable request. The raw data used for the data diagrams in the main figures are available in <https://doi.org/10.6084/m9.figshare.14511885.v192>.

Code availability

Simulation trajectories were collected using NAMD and ARBD. Visualization and analysis were performed using VMD and Python. All of these software packages are publicly available.

Received: 23 November 2020; Accepted: 6 May 2021;

Published online: 03 June 2021

References

- Rostovtseva, T. & Colombini, M. ATP flux is controlled by a voltage-gated channel from the mitochondrial outer membrane. *J. Biol. Chem.* **271**, 28006–28008 (1996).
- Camara, A. K. S., Zhou, Y. F., Wen, P. C., Tajkhorshid, E. & Kwok, W. M. Mitochondrial VDAC1: a key gatekeeper as potential therapeutic target. *Front. Physiol.* **8**, 640 (2017).
- Hodge, T. & Colombini, M. Regulation of metabolite flux through voltage-gating of VDAC channels. *J. Membr. Biol.* **157**, 271–279 (1997).
- Pastorino, J. G., Shulga, N. & Hoek, J. B. Mitochondrial binding of hexokinase II inhibits Bax-induced cytochrome c release and apoptosis. *J. Biol. Chem.* **277**, 7610–7618 (2002).
- Doran, E. & Halestrap, A. P. Cytochrome c release from isolated rat liver mitochondria can occur independently of outer-membrane rupture: possible role of contact sites. *Biochem. J.* **348**, 343–350 (2000).
- Shimizu, S., Matsuoka, Y., Shinohara, Y., Yoneda, Y. & Tsujimoto, Y. Essential role of voltage-dependent anion channel in various forms of apoptosis in mammalian cells. *J. Cell Biol.* **152**, 237–250 (2001).
- Azoulay-Zohar, H., Israelson, A., Salah, A.-H. & Shoshan-Barmatz, V. In self-defence: hexokinase promotes voltage-dependent anion channel closure and prevents mitochondria-mediated apoptotic cell death. *Biochem. J.* **377**, 347–355 (2004).
- Zhou, H. et al. Mff-dependent mitochondrial fission contributes to the pathogenesis of cardiac microvasculature ischemia/reperfusion injury via induction of mROS-mediated cardiolipin oxidation and HK2/VDAC1 disassociation-involved mPTP opening. *J. Am. Heart Assoc.* **6**, e005328 (2017).
- Arbel, N., Ben-Hail, D. & Shoshan-Barmatz, V. Mediation of the antiapoptotic activity of Bcl-xL protein upon interaction with VDAC1 protein. *J. Biol. Chem.* **287**, 23152–23161 (2012).
- Banerjee, J. & Ghosh, S. Bax increases the pore size of rat brain mitochondrial voltage-dependent anion channel in the presence of tBid. *Biochem. Biophys. Res. Commun.* **323**, 310–314 (2004).
- Kumarswamy, R. & Chandna, S. Putative partners in Bax mediated cytochrome-c release: ANT, CypD, VDAC or none of them? *Mitochondrion* **9**, 1–8 (2009).
- Martel, C., Wang, Z. & Brenner, C. VDAC phosphorylation, a lipid sensor influencing the cell fate. *Mitochondrion* **19**, 69–77 (2014).
- Lan, C. H. et al. Involvement of VDAC1 and Bcl-2 family of proteins in VacA-induced cytochrome c release and apoptosis of gastric epithelial carcinoma cells. *J. Dig. Dis.* **11**, 43–49 (2010).
- Roy, S. S. et al. Bad targets the permeability transition pore independent of Bax or Bak to switch between Ca^{2+} -dependent cell survival and death. *Mol. Cell* **33**, 377–388 (2009).
- Tomasello, F. et al. Outer membrane VDAC1 controls permeability transition of the inner mitochondrial membrane *in cellulo* during stress-induced apoptosis. *Cell Res.* **19**, 1363–1367 (2009).
- Arora, K. & Pedersen, P. L. Functional significance of mitochondrial bound hexokinase in tumor cell metabolism: evidence for preferential phosphorylation of glucose by intramitochondrially generated ATP. *J. Biol. Chem.* **263**, 17422–17428 (1988).
- Rempel, A., Mathupala, S., Griffin, C. A., Hawkins, A. L. & Pedersen, P. L. Glucose catabolism in cancer cells: amplification of the gene. *Cancer Res.* **56**, 2468–2471 (1996).
- Bryson, J. M., Coy, P. E., Gottlob, K., Hay, N. & Robey, R. B. Increased hexokinase activity, of either ectopic or endogenous origin, protects renal epithelial cells against acute oxidant-induced cell death. *J. Biol. Chem.* **277**, 11392–11400 (2002).
- Gottlob, K. et al. Inhibition of early apoptotic events by Akt/PKB is dependent on the first committed step of glycolysis and mitochondrial hexokinase. *Genes Dev.* **15**, 1406–1418 (2001).
- Wilson, J. E. Isozymes of mammalian hexokinase: structure, subcellular localization and metabolic function. *J. Exp. Biol.* **206**, 2049–2057 (2003).
- Abu-Hamad, S., Zaid, H., Israelson, A., Nahon, E. & Shoshan-Barmatz, V. Hexokinase-I protection against apoptotic cell death is mediated via interaction with the voltage-dependent anion channel-1: mapping the site of binding. *J. Biol. Chem.* **283**, 13482–13490 (2008).
- Shoshan-Barmatz, V., Ben-Hail, D., Admoni, L., Krelin, Y. & Tripathi, S. S. The mitochondrial voltage-dependent anion channel 1 in tumor cells. *Biochim. Biophys. Acta Biomembr.* **1848**, 2547–2575 (2015).
- Maldonado, E. N. & Lemasters, J. J. Warburg revisited: regulation of mitochondrial metabolism by voltage-dependent anion channels in cancer cells. *J. Pharmacol. Exp. Ther.* **342**, 637–641 (2012).
- Ehsani-Zonouz, A., Golestani, A. & Nemat-Gorgani, M. Interaction of hexokinase with the outer mitochondrial membrane and a hydrophobic matrix. *Mol. Cell. Biochem.* **223**, 81–87 (2001).
- Goldin, N. et al. Methyl jasmonate binds to and detaches mitochondria-bound hexokinase. *Oncogene* **27**, 4636–4643 (2008).
- Shoshan-Barmatz, V. & Golan, M. Mitochondrial VDAC1: function in cell life and death and a target for cancer therapy. *Curr. Med. Chem.* **19**, 714–735 (2012).
- Simamura, E., Shimada, H., Hatta, T. & Hirai, K.-I. Mitochondrial voltage-dependent anion channels (VDACs) as novel pharmacological targets for anti-cancer agents. *J. Bioenerg. Biomembr.* **40**, 213–217 (2008).
- Wenner, C. E. Targeting mitochondria as a therapeutic target in cancer. *J. Cell. Physiol.* **227**, 450–456 (2012).
- Krasnov, G. S., Dmitriev, A. A., Lakunina, V. A., Kirpiy, A. A. & Kudryavtseva, A. V. Targeting VDAC-bound hexokinase II: a promising approach for concomitant anti-cancer therapy. *Expert Opin. Ther. Targets* **17**, 1221–1233 (2013).
- Ko, Y. et al. A translational study “case report” on the small molecule “energy blocker” 3-bromopyruvate (3BP) as a potent anticancer agent: from bench side to bedside. *J. Bioenerg. Biomembr.* **44**, 163–170 (2012).
- Zaid, H., Abu-Hamad, S., Israelson, A., Nathan, I. & Shoshan-Barmatz, V. The voltage-dependent anion channel-1 modulates apoptotic cell death. *Cell Death Differ.* **12**, 751 (2005).
- Shoshan-Barmatz, V., Zakar, M., Rosenthal, K. & Abu-Hamad, S. Key regions of VDAC1 functioning in apoptosis induction and regulation by hexokinase. *Biochim. Biophys. Acta Biomembr.* **1787**, 421–430 (2009).
- Arzoin, L., Zilberberg, N., Ben-Romano, R. & Shoshan-Barmatz, V. Voltage-dependent anion channel 1-based peptides interact with hexokinase to prevent its anti-apoptotic activity. *J. Biol. Chem.* **284**, 3946–3955 (2009).
- Abu-Hamad, S. et al. The VDAC1 N-terminus is essential both for apoptosis and the protective effect of anti-apoptotic proteins. *J. Cell Sci.* **122**, 1906–1916 (2009).
- Pastorino, J. G., Hoek, J. B. & Shulga, N. Activation of glycogen synthase kinase β disrupts the binding of hexokinase II to mitochondria by phosphorylating voltage-dependent anion channel and potentiates chemotherapy-induced cytotoxicity. *Cancer Res.* **65**, 10545–10554 (2005).
- Rosano, C. Molecular model of hexokinase binding to the outer mitochondrial membrane porin (VDAC1): implication for the design of new cancer therapies. *Mitochondrion* **11**, 513–519 (2011).
- Zhang, D., Yip, Y. M. & Li, L. *In silico* construction of HK2-VDAC1 complex and investigating the HK2 binding-induced molecular gating mechanism of VDAC1. *Mitochondrion* **30**, 222–228 (2016).
- Ujwal, R. et al. The crystal structure of mouse VDAC1 at 2.3 Å resolution reveals mechanistic insights into metabolite gating. *Proc. Natl. Acad. Sci. USA* **105**, 17742–17747 (2008).
- Xie, G. & Wilson, J. E. Rat brain hexokinase: the hydrophobic N-terminus of the mitochondrially bound enzyme is inserted in the lipid bilayer. *Arch. Biochem. Biophys.* **267**, 803–810 (1988).
- Pastorino, J. G. & Hoek, J. B. Regulation of hexokinase binding to VDAC. *J. Bioenerg. Biomembr.* **40**, 171–182 (2008).

41. Neumann, D., Bückers, J., Kastrop, L., Hell, S. W. & Jakobs, S. Two-color STED microscopy reveals different degrees of colocalization between hexokinase-I and the three human VDAC isoforms. *PMC Biophys.* **3**, 4 (2010).
42. Bryan, N. & Raich, K. P. Identification of a mitochondrial-binding site on the N-terminal end of hexokinase II. *Biosci. Rep.* **35**, e00205 (2015).
43. Sun, L., Shukair, S., Naik, T. J., Moazed, F. & Ardehali, H. Glucose phosphorylation and mitochondrial binding are required for the protective effects of hexokinases I and II. *Mol. Cell. Biol.* **28**, 1007–1017 (2008).
44. Ladislav Kováč, B. D. N. & Ernster, L. A method for determining the intracellular distribution of enzymes in yeast provides no evidence for the association of hexokinase with mitochondria. *Biochem. Biophys. Res. Commun.* **134**, 285–291 (1986).
45. Kurokawa, M., Yokoyama, K., Kaneko, M. & Ishibashi, S. Difference in hydrophobicity between mitochondria-bindable and non-bindable forms of hexokinase purified from rat brain. *Biochem. Biophys. Res. Commun.* **115**, 1101–1107 (1983).
46. Ohkubo, Y. Z., Pogorelov, T. V., Arcario, M. J., Christensen, G. A. & Tajkhorshid, E. Accelerating membrane insertion of peripheral proteins with a novel membrane mimetic model. *Biophys. J.* **102**, 2130–2139 (2012).
47. Bergdoll, L. A. et al. Protonation state of glutamate 73 regulates the formation of a specific dimeric association of mVDAC1. *Proc. Natl Acad. Sci. USA* **115**, E172–E179 (2018).
48. Cheng, Q., Sedlic, F., Pravdic, D., Bosnjak, Z. J. & Kwok, W.-M. Biphasic effect of nitric oxide on the cardiac voltage-dependent anion channel. *FEBS Lett.* **585**, 328–334 (2011).
49. Zhao, X. et al. Phosphoproteome analysis of functional mitochondria isolated from resting human muscle reveals extensive phosphorylation of inner membrane protein complexes and enzymes. *Mol. Cell. Proteom.* **10**, M110–299 (2011).
50. Beurel, E. & Jope, R. S. The paradoxical pro- and anti-apoptotic actions of GSK3 in the intrinsic and extrinsic apoptosis signaling pathways. *Prog. Neurobiol.* **79**, 173–189 (2006).
51. Das, S., Steenberg, C. & Murphy, E. Does the voltage dependent anion channel modulate cardiac ischemia-reperfusion injury? *Biochim. Biophys. Acta Biomembr.* **1818**, 1451–1456 (2012).
52. Kerner, J., Lee, K., Tandler, B. & Hoppel, C. L. VDAC proteomics: post-translation modifications. *Biochim. Biophys. Acta Biomembr.* **1818**, 1520–1525 (2012).
53. Schwartz, H. et al. Myocardial ischemia/reperfusion causes VDAC phosphorylation which is reduced by cardioprotection with a p38 MAP kinase inhibitor. *Proteomics* **7**, 4579–4588 (2007).
54. Majewski, N. et al. Hexokinase-mitochondria interaction mediated by Akt is required to inhibit apoptosis in the presence or absence of Bax and Bak. *Mol. Cell* **16**, 819–830 (2004).
55. Sutherland, C. What are the *bona fide* GSK3 substrates? *Int. J. Alzheimer's Disease* **2011**, 505607 (2011).
56. Stamos, J. L., Chu, M. L.-H., Enos, M. D., Shah, N. & Weis, W. I. Structural basis of GSK-3 inhibition by N-terminal phosphorylation and by the Wnt receptor LRP6. *eLife* **3**, e01998 (2014).
57. Doble, B. W. & Woodgett, J. R. GSK-3: tricks of the trade for a multi-tasking kinase. *J. Cell Sci.* **116**, 1175–1186 (2003).
58. Xie, G. & Wilson, J. E. Tetrameric structure of mitochondrially bound rat brain hexokinase: a crosslinking study. *Arch. Biochem. Biophys.* **276**, 285–293 (1990).
59. Robey, R. & Hay, N. Mitochondrial hexokinases, novel mediators of the antiapoptotic effects of growth factors and akt. *Oncogene* **25**, 4683–4696 (2006).
60. Zalk, R., Israelson, A., Garty, E. S., Azoulay-Zohar, H. & Shoshan-Barmatz, V. Oligomeric states of the voltage-dependent anion channel and cytochrome c release from mitochondria. *Biochem. J.* **386**, 73–83 (2005).
61. Hoogenboom, B. W., Suda, K., Engel, A. & Fotiadis, D. The supramolecular assemblies of voltage-dependent anion channels in the native membrane. *J. Mol. Biol.* **370**, 246–255 (2007).
62. Sali, A. & Blundell, T. L. Comparative protein modelling by satisfaction of spatial restraints. *J. Mol. Biol.* **234**, 779–815 (1993).
63. Lin, K., Simossis, V. A., Taylor, W. R. & Heringa, J. A simple and fast secondary structure prediction method using hidden neural networks. *Bioinformatics* **21**, 152–159 (2004).
64. Fiser, A. & Do, R. K. G. et al. Modeling of loops in protein structures. *Protein Sci.* **9**, 1753–1773 (2000).
65. Rostkowski, M., Olsson, M., Sondergaard, C. & Jensen, J. Graphical analysis of pH-dependent properties of proteins predicted using PROPKA. *BMC Struct. Biol.* **11**, 6 (2011).
66. Olsson, M. H., Søndergaard, C. R., Rostkowski, M. & Jensen, J. H. PROPKA3: consistent treatment of internal and surface residues in empirical pKa predictions. *J. Chem. Theory Comput.* **7**, 525–537 (2011).
67. Susanne E. Horvath, G. D. Lipids of mitochondria. *Prog. Lipid Res.* **52**, 590–614 (2013).
68. Qi, Y. et al. CHARMM-GUI HMMM builder for membrane simulations with the highly mobile membrane-mimetic model. *Biophys. J.* **109**, 2012–2022 (2015).
69. Jorgensen, W. L., Chandrasekhar, J., Madura, J. D., Impey, R. W. & Klein, M. L. Comparison of simple potential functions for simulating liquid water. *J. Chem. Phys.* **79**, 926–935 (1983).
70. Muller, M. P., Wang, Y., Morrissey, J. H. & Tajkhorshid, E. Lipid specificity of the membrane binding domain of coagulation factor X. *J. Thromb. Haem.* **15**, 2005–2016 (2017).
71. Vermaas, J. V. et al. Efficient exploration of membrane-associated phenomena at atomic resolution. *J. Membr. Biol.* **248**, 563–582 (2015).
72. Tietjen, G. T. et al. Coupling X-ray reflectivity and *in silico* binding to yield dynamics of membrane recognition by Tim1. *Biophys. J.* **113**, 1505–1519 (2017).
73. Jo, S., Kim, T., Iyer, V. G. & Im, W. CHARMM-GUI: a web-based graphical user interface for charmm. *J. Comput. Chem.* **29**, 1859–1865 (2008).
74. Phillips, J. C. et al. Scalable molecular dynamics with NAMD. *J. Comput. Chem.* **26**, 1781–1802 (2005).
75. Phillips, J. C. et al. Scalable molecular dynamics on CPU and GPU architectures with NAMD. *J. Chem. Phys.* **153**, 044130 (2020).
76. Huang, J. et al. CHARMM36m: an improved force field for folded and intrinsically disordered proteins. *Nat. Methods* **14**, 71–73 (2017).
77. Klauda, J. B. et al. Update of the CHARMM all-atom additive force field for lipids: Validation on six lipid types. *J. Phys. Chem. B* **114**, 7830–7843 (2010).
78. Darden, T., York, D. & Pedersen, L. Particle mesh Ewald: an $N \cdot \log(N)$ method for Ewald sums in large systems. *J. Chem. Phys.* **98**, 10089–10092 (1993).
79. Martyna, G. J., Tobias, D. J. & Klein, M. L. Constant pressure molecular dynamics algorithms. *J. Chem. Phys.* **101**, 4177–4189 (1994).
80. Feller, S. E., Zhang, Y. & Pastor, R. W. Constant pressure molecular dynamics simulation: the Langevin piston method. *J. Chem. Phys.* **103**, 4613–4621 (1995).
81. Humphrey, W., Dalke, A. & Schulten, K. VMD: visual molecular dynamics. *J. Mol. Graph.* **14**, 33–38 (1996).
82. Comer, J. & Aksimentiev, A. Predicting the DNA sequence dependence of nanopore ion current using atomic-resolution Brownian dynamics. *J. Phys. Chem. C* **116**, 3376–3393 (2012).
83. de la Torre, J. G., Huertas, M. L. & Carrasco, B. Calculation of hydrodynamic properties of globular proteins from their atomic-level structure. *Biophys. J.* **78**, 719–730 (2000).
84. Baker, N. A., Sept, D., Joseph, S., Holst, M. J. & McCammon, J. A. Electrostatics of nanosystems: application to microtubules and the ribosome. *Proc. Natl Acad. Sci. USA* **98**, 10037–10041 (2001).
85. Fogolari, F., Brigo, A. & Molinari, H. The Poisson–Boltzmann equation for biomolecular electrostatics: a tool for structural biology. *J. Mol. Recognit.* **15**, 377–392 (2002).
86. Im, W., Beglov, D. & Roux, B. Continuum solvation model: computation of electrostatic forces from numerical solutions to the poisson-boltzmann equation. *Comput. Phys. Commun.* **111**, 59–75 (1998).
87. Singharoy, A. et al. Atoms to phenotypes: molecular design principles of cellular energy metabolism. *Cell* **179**, 1098–1111 (2019).
88. McGuffee, S. R. & Elcock, A. H. Diffusion, crowding & protein stability in a dynamic molecular model of the bacterial cytoplasm. *PLoS Comput. Biol.* **6**, e1000694 (2010).
89. Cohen, J., Arkhipov, A., Braun, R. & Schulten, K. Imaging the migration pathways for O₂, CO, NO, and Xe inside myoglobin. *Biophys. J.* **91**, 1844–1857 (2006).
90. Van Zundert, G. et al. The HADDOCK2.2 web server: user-friendly integrative modeling of biomolecular complexes. *J. Mol. Biol.* **428**, 720–725 (2016).
91. Heyer, L. J., Kruglyak, S. & Yooseph, S. Exploring expression data: identification and analysis of coexpressed genes. *Genome Res.* **9**, 1106–1115 (1999).
92. Haloi, N. Datasets supporting Haloi et al. *Commun. Biol.* figshare. dataset <https://doi.org/10.6084/m9.figshare.14511885.v1> (2021).
93. Jo, S., Vargyas, M., Vasko-Szedlar, J., Roux, B. & Im, W. PBEQ-Solver for online visualization of electrostatic potential of biomolecules. *Nucleic Acids Res.* **36**, W270–W275 (2008).
94. Waskom, M. & the seaborn development team. *mwaskom/seaborn*. <https://doi.org/10.5281/zenodo.592845> (2020).
95. Smart, O. S., Neduveilil, J. G., Wang, X., Wallace, B. & Sansom, M. S. HOLE: a program for the analysis of the pore dimensions of ion channel structural models. *J. Mol. Graph.* **14**, 354–360 (1996).

Acknowledgements

We thank Christopher Maffeo (UIUC) for insightful conversations and assistance in designing Brownian dynamics simulations. This research was supported by the National Institutes of Health grants R01-HL131673 (to W.-M.K., A.K.S.C., and E.T.), and P41-GM104601 (to E.T.). Simulations in this study have been performed using allocations at National Science Foundation Supercomputing Centers (XSEDE grant number MCA06N060) and the Blue Waters supercomputer of National Center for Supercomputing Applications at University of Illinois at Urbana-Champaign.

Author contributions

N.H., P.-C.W., A.K.S.C., W.-M.K., and E.T. designed research; N.H., Q.C., M.Y., and G.N. performed research; N.H., P.-C.W., and W.-M.K. analyzed data; and N.H., P.-C.W., W.-M.K., and E.T. wrote the paper.

Competing interests

The authors declare no competing interests.

Additional information

Supplementary information The online version contains supplementary material available at <https://doi.org/10.1038/s42003-021-02205-y>.

Correspondence and requests for materials should be addressed to W.-M.K. or E.T.

Reprints and permission information is available at <http://www.nature.com/reprints>

Publisher's note Springer Nature remains neutral with regard to jurisdictional claims in published maps and institutional affiliations.



Open Access This article is licensed under a Creative Commons Attribution 4.0 International License, which permits use, sharing, adaptation, distribution and reproduction in any medium or format, as long as you give appropriate credit to the original author(s) and the source, provide a link to the Creative Commons license, and indicate if changes were made. The images or other third party material in this article are included in the article's Creative Commons license, unless indicated otherwise in a credit line to the material. If material is not included in the article's Creative Commons license and your intended use is not permitted by statutory regulation or exceeds the permitted use, you will need to obtain permission directly from the copyright holder. To view a copy of this license, visit <http://creativecommons.org/licenses/by/4.0/>.

© The Author(s) 2021